Journal of Materials Chemistry C

PAPER

View Article Online
View Journal | View Issue

Open Access Article. Published on 27 June 2017. Downloaded on 8/31/2025 5:52:32 AM.
This article is licensed under a Creative Commons Attribution-NonCommercial 3.0 Unported Licence.

Check for updates

Cite this: J. Mater. Chem. C, 2017, 5, 7969

Fluoride-sulfophosphate glasses as hosts for broadband optical amplification through transition metal activators†

W. C. Wang,[ab] Q. H. Le,[a] Q. Y. Zhang [b] and L. Wondraczek *[a]

Received 28th April 2017,
Accepted 26th June 2017

DOI: 10.1039/c7tc01853c

rsc.li/materials-c

Unusually stable multi-anion glasses of the fluoride-sulfophosphate type (FPS) are introduced as a new host material for optically active cation species. Despite a notoriously low polymerization grade, anion mixing in this glass system enables facile manufacture of bulk or fiber devices which combine several advantages of fluoride and phosphate glasses while using the stabilizing effect of sulfate additions. Using the example of chromium doping, we demonstrate broad red photoluminescence at 734 nm and inhomogeneous broadening of the *R*-line at 694 nm, originating from the $^4T_2 \rightarrow {}^4A_2$ and $^2E \rightarrow {}^4A_2$ transitions of Cr^{3+}, respectively. The luminescence mechanism is further analyzed on the basis of the corresponding Tanabe–Sugano diagram. Tailored through chemical composition, internally nucleated precipitation of a nanocrystalline fluoride phase enables switching between high-field and low-field configurations of the Cr^{3+} ion, resulting in the specific emission properties and setting the path towards FPS-based optical devices.

1. Introduction

Transition metal doped glasses have been receiving continuous attention in the quest for new tunable fiber lasers.[1,2] In particular, different chromium ions have been considered as interesting species, taking into account their prominent role in crystalline laser gain media, *e.g.*, Cr^{3+} in ruby lasers,[3] Cr^{4+} in YAG and forsterite,[4] or Cr^{2+} in the chalcogenide matrix.[5] While chromium ions occur in a broad variety of valence states (ranging from "+1" to "+6"), in oxide glasses, only Cr^{3+}, Cr^{5+} and Cr^{6+} are typically found.[6–8] Of particular interest are the broad near-infrared emission bands and the narrow visible emission bands which derive from the $^4T_2$ level (low-field sites) and the ^2E level (high-field sites) of Cr^{3+}, respectively. Their energetic position is dominated by the ligand-dependence of the underlying *d–d* transition.[9–11] Broadband emission at approximately 900 nm, originating from Cr^{3+} ions in a phosphate glass matrix, was reported by Sharp *et al.* as early as 1969.[12] Since then, many authors have been considering the subject. For example, Murata *et al.* provided a systematic study on the relationship of composition and redox reactions among chromium ions in multicomponent oxide glasses, reporting a redox shift from Cr^{3+} to Cr^{6+} with increasing matrix basicity.[13] Also in the form of optical fibers, significant progress has been made. For example, Cr^{3+}-doped silica fibers with a gain bandwidth covering the entire transmission range of low loss and low dispersion windows were reported in 2012, aimed at increasing the data transmission capacity in the next generation of optical communication systems.[14] Cr^{3+}-doped glass ceramic fibers were also demonstrated for potential application in broadband tunable fiber lasers.[15] However, despite these milestone findings, the preparation of efficient fiber lasers from a Cr^{3+}-doped glass has not yet been successful. Therefore, the search for suitable host materials continues.

Traditionally, phosphate glasses have been among the most prominent choices as host species for solid-state (glass) lasers, primarily due to high rare earth solubility and low phonon energy.[16–18] The structural backbone of these materials comprises a network of PO_4 tetrahedra in which three of the oxygen species provide the ability to link to a neighboring tetrahedron, while the remaining anion is linked to the central phosphorous *via* a double bond. This configuration is the fundamental basis for the specific optical properties of phosphate glasses, in particular, electronic polarizability. Secondary cation species (including rare earth or transition metal ions) can be added to this ensemble as so-called modifiers, that is, introducing chemical bonds with a more ionic character. Then, in order to charge-balance these modifier ions, not all three available edges of the phosphate tetrahedron are interconnecting, but non-bridging oxygen species are formed which interrupt the

[a] Otto Schott Institute of Materials Research, Friedrich Schiller University Jena, Fraunhoferstraße 6, 07743 Jena, Germany. E-mail: lothar.wondraczek@uni-jena.de
[b] State Key Laboratory of Luminescent Materials and Devices, Guangdong Provincial Key Laboratory of Fiber Laser Materials and Applied Techniques, and Institute of Optical Communication Materials, South China University of Technology, Guangzhou 510641, P. R. China

† Electronic supplementary information (ESI) available. See DOI: 10.1039/c7tc01853c

Open Access Article. Published on 27 June 2017. Downloaded on 8/31/2025 5:52:32 AM.
This article is licensed under a Creative Commons Attribution-NonCommercial 3.0 Unported Licence.

phosphate network. This is expressed in the *Q*-group nomenclature, where $Q^{n=0...3}$ refers to a phosphate entity with n bridging oxygen species. If $n = 2$ (the metaphosphate composition), the network comprises phosphate chains and/or rings. For $n > 2$ (ultraphosphates), these chains are crosslinked. When $n = 0...1$ (pyro-/orthophosphates), the glass comprises isolated phosphate islands in an ionic matrix. The modifying species locate between the super-structural units. Depending on charge, size and electronic structure, they interact with the local phosphate network to a different extent. Furthermore, non-linear cross-interaction among the cations leads to specific mixing effects, which are frequently made use of in the design of certain macroscopic properties.[19–21] It was found that the stability of phosphate glasses can be enhanced significantly through the introduction of sulfate anions, $[SO_4]^{2-}$, both in terms of rheology (liquid fragility) and chemical properties (corrosion resistance).[22–24] Beyond this immediate, practical interest, these sulfophosphate glasses have also been identified as interesting host species for transition metal ions as they provide a very peculiar local environment of sulfate as well as phosphate entities in which ligand field splitting and local redox deviate from conventional molecular field considerations.[23,25] However, especially at high sulfate content, liquid–liquid phase separation has been observed, which prevents their use as fiber or bulk optical materials.[26]

In the present study, this leads to further extension of this chemical system by adding fluoride as another structural entity, creating fluoride-sulfophosphate glasses (FPS). As a well-known counterpart, fluorophosphate (FP) glasses combine many properties which are desired in high-performance optical applications, *e.g.*, high optical transmittance across the ultraviolet (UV) to near-infrared (NIR) spectral range, very low partial dispersion and linear and non-linear refractive index[27] (thus, high laser damage threshold), low phonon energy and the ability of incorporating large amounts of optically active species, based on the chemical and electrical properties of the fluoride anion relative to those of oxygen. Applications have been evolving on the basis of these properties primarily on the areas of (passive) optical lenses, fiber optical amplifiers, lasers and frequency converters,[28,30] with current research focusing on the effects of mixed doping with various rare earth species,[31] and also on modifying the glass matrix through the addition of further anion species.[27,32,33] For example, Kumar *et al.* studied the effect of sulfate and borate additions on the optical properties of FP glasses, reporting that sulfate acts positively on luminescence efficiency of rare earth dopants.[34,35] Important in these considerations, when the introduction of new anion species leads to an improvement of thermal stability or, *e.g.*, mechanical performance, it must not adversely affect the spectroscopic properties of the dopant species. With this in mind, FPS glasses provide an extremely complex structural environment to optically active dopant species and, according to recent findings,[36] surprising glass stability and a broad processing window. Here, we exploit these properties in a new host material for chromium-based broadband optical activity. We compare a series of Cr^{3+}-doped FPS glasses to their sulfate-free FP counterparts with varying F : P : S and F : P ratios, respectively, by means of assessing their structural and optical properties. This shows that FPS glasses provide a promising material towards broadband tunable fiber lasers.

2. Experimental

Two sets of glasses were considered in the present study, *i.e.*, a fluoride sulfophosphate (FPS) and a reference fluorophosphate (FP) series. Molar compositions were selected by starting from alkaline earth FP, $(100 - x)(MgF_2, CaF_2, SrF_2, AlF_3) - xSr(PO_3)_2$ (x = 0, 2, 4, 10, 15; denoted FP0, FP2, FP4, FP10, and FP15, respectively),[27–29] and subsequently replacing $Sr(PO_3)_2$ in the FP15 composition by $SrSO_4$, $85(MgF_2, CaF_2, SrF_2, AlF_3) - (15 - y)Sr(PO_3)_2 - ySrSO_4$ (y = 5, 7.5, 10, 15; denoted as FP10S5, FP7.5S7.5, FP5S10, and FP0S15, respectively). All glasses were doped by adding 0.05 mol% Cr_2O_3. Only $Sr(PO_3)_2$ was dried at 120 °C for 7 h before weighting, then 100 g batches using high purity raw materials were thoroughly mixed in a plastic bottle. Batches of 100 g were melted in a muffle furnace, in Pt crucibles at 1000–1100 °C for 2 h, cooled to 830–950 °C and poured into a preheated graphite mold. The subsequent annealing process was carried out at 440–510 °C for another 2 h, followed by cooling to room temperature at the furnace rate ($\sim$2 K min^{-1}). Deviating from this procedure, the compositions with poor glass forming ability (FP0, FP2, FP5S10 and FP0S15) were prepared through rapid quenching by pouring the melt onto cold copper plates and immediate pressing with another copper stamp. Subsequently, annealing of these samples followed the same procedure as above. After annealing, the glass samples which were obtained through the regular method were cut into two types of specimens, *i.e.*, 20 mm × 10 mm × 1 mm and 20 mm × 10 mm × 5 mm, and both sides were polished for further spectroscopic analyses and mechanical analyses, respectively. For the quenched samples of FP2 and FP5S10, the obtained plates were polished directly without further cutting. In the case of FP0 and FP0S15, polishing was not possible because the samples were too thin (0.5–0.6 mm), so that spectroscopic analyses were performed directly on unpolished samples. Remaining glass shards were ground and sieved for differential thermal analysis (DTA) and X-ray diffraction (XRD) analysis.

The glass density was tested through the Archimedes method at 20.5 °C using distilled water as the immersion liquid. XRD was conducted on a MiniFlex600 (Rigaku, Japan) X-ray diffractometer with Cu-Kα radiation (λ = 1.5406 Å) at a tube voltage of 40 kV and a tube current of 15 mA. The glass refractive index was evaluated with a Pulfrich refractometer on samples with a thickness of 5 mm. UV-Vis-NIR absorption spectra were recorded on a Cary 5000 (Agilent) double-beam spectrophotometer with a spectral resolution of 1.0 nm. The glass transition and characteristic temperatures of crystallization were analyzed on a Differential Thermal Analyzer instrument assembled by our laboratory. Structural analyses were done by Raman spectroscopy (Renishaw, UK) using a 488 nm Argon laser as the excitation source. Static luminescence spectra were recorded on a high-resolution spectrofluorometer (Fluorolog, Horiba Jobin-Yvon), using a continuous

 This journal is © The Royal Society of Chemistry 2017

Open Access Article. Published on 27 June 2017. Downloaded on 8/31/2025 5:52:32 AM.
This article is licensed under a Creative Commons Attribution-NonCommercial 3.0 Unported Licence.

wave 450 W Xe lamp as the excitation source and a Hamamatsu R2658P photomultiplier tube for detection.

Finally, the elastic properties were characterized by ultrasonic echography on co-planar, optically polished glass plates. The longitudinal and transversal wave velocities, c_L and c_T, were determined with a piezoelectric transducer operating at frequencies of 8–12 MHz (Echometer 1077, Karl Deutsch GmbH & Co KG).

All measurements were performed at room temperature.

3. Results and discussion

3.1. Glass formation, optical absorption and basic physical properties

As noted in the Experimental section, with the exception of the low- or no-phosphate candidates, all compositions were readily cooled into visually transparent glasses without visible bubbles, inclusions or signs of crystallization. Sample photographs are provided in the inset of Fig. 1. As expected, Cr^{3+}-doping resulted in a green tint with increasing saturation for increasing phosphate content. For FP2 and FP5S10, the green appearance evolves into a light yellowish shade, and turns to red for FP0 and FP0S15. In the latter two samples, some turbidity is seen, indicating that these samples comprise at least two phases. The red color is similar to that of ruby, where it is caused by Cr^{3+} in the alkali matrix α-Al_2O_3, in a strained six-fold coordination.[37] This implies that also in the present case, Cr^{3+} ions enter into the strong ligand field of a crystalline precipitate.[38,39] Fig. 1 shows the UV-NIR absorption spectra which correspond to the above observations. In the regularly cast samples, there are two broad absorption bands, *i.e.*, at 439 nm and 640 nm, associated with the characteristic Cr^{3+}: $^4A_2 \rightarrow {}^4T_1$ and Cr^{3+}: $^4A_2 \rightarrow {}^4T_2$ transitions. A zoom at the red region reveals two distinct shoulder bands at ~647 nm and 680 nm, corresponding to Cr^{3+}: $^2T_1 \rightarrow {}^4A_2$ and Cr^{3+}: $^4A_2 \rightarrow {}^2E$ (see Fig. S1 in the ESI†). In addition to this, a further intense absorption band is observed at ~251 nm, attributed to the charge transfer state of Cr^{6+}, indicating a strongly oxidizing effect in the quenched samples, which leads to the formation of hexavalent chromium, Cr^{6+}.

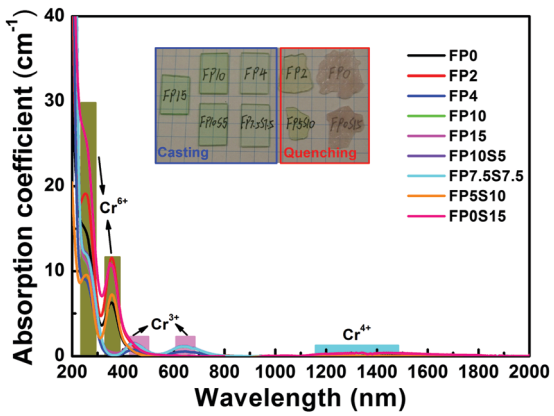

Fig. 1 Optical absorption spectra of chromium-doped FP and FPS glasses. The inset shows sample photographs (mesh spacing of 5 mm).

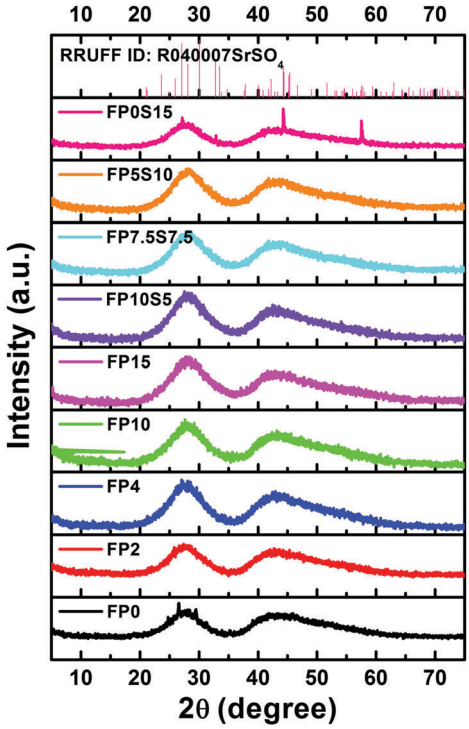

Fig. 2 XRD patterns of the chromium doped FP and FPS samples.

Noteworthily, further absorption peaks which could be characteristic of Cr^{4+} (in the spectral range of 1000–2000 nm) are detected in the quenched samples.

XRD was employed to verify the phase assembly of all samples. Diffraction patterns are shown in Fig. 2. For all samples, data are dominated by two broad, amorphous humps which reflect the glassy state. With the exceptions of FP0 and FP0S15, there are no sharp peaks which would indicate the presence of a secondary, crystalline phase. In the latter two samples, such peaks are present, that is, they are at least partially crystallized (what is in accordance with the previous optical inspection). Using Scherer's equation, a crystallite size of ~30–50 nm is approximated from the width of those diffraction peaks. Assignment to one or more specific crystallite phases is presently not possible due to the apparently low crystallite volume fraction and the unavailability of unambiguous reference data. Tentatively, a Celestine-type phase is identified in FP0S15, $SrSO_4$. For FP0, we expect one or more alkaline earth fluoride phases. Here, we speculate that the crystallite species comprise fluoride (FP0 and FP0S15) and sulfide compounds (FP0S15), subject to future analysis of the specific crystallization mechanism. The low crystallite size, high sample transparency and apparent internal nucleation suggest further exploration of corresponding glass ceramics, however, beyond the scope of the present study.

The selected physical properties of the two glass series are summarized in Table 1. Upon increasing the content of phosphate, the density of the present glasses continuously increases, *i.e.*, from 3.454 g cm^{-3} to 3.503 g cm^{-3}. When $Sr(PO_3)_2$ is replaced by $SrSO_4$, the density monotonically increases.

Open Access Article. Published on 27 June 2017. Downloaded on 8/31/2025 5:52:32 AM.
This article is licensed under a Creative Commons Attribution-NonCommercial 3.0 Unported Licence.

Table 1 Physical properties of FP and FPS glasses

Glass	Density (g cm^{-3})	Refractive index (±0.0005) $n_{C'}$(643.84)	n_d(587.56)	n_e(546.06)	$n_{F'}$(479.98)	n_h(435.84)	Abbe's number	Thermal parameters T_g	T_x	T_p	Cutoff wavelength (nm)	Urbach energy (eV)	Λth	Elastic modulus (GPa)
FP0	3.454	—	—	—	—	—	—	403	460	475	—	—	0.349	—
FP2	3.472	—	—	—	—	—	—	421	498	514	395	1.31	0.356	—
FP4	3.457	—	—	—	—	—	—	427	523	541	282	2.87	0.374	73.1 ± 0.6
FP10	3.427	1.4638	1.4652	1.4663	1.4690	1.4714	89.8 ± 17.3	445	—	—	294	3.57	0.390	76.3 ± 0.7
FP15	3.503	1.4896	1.4911	1.4925	1.4956	1.4985	81.9 ± 6.8	467	—	—	292	3.23	0.432	77.4 ± 0.7
FP10S5	3.527	1.4801	1.4816	1.4829	1.4871	1.4884	69.5 ± 5.0	448	—	—	296	3.59	0.388	75.4 ± 0.7
FP7.5S7.5	3.531	1.4726	1.4740	1.4753	1.4781	1.4808	86.1 ± 7.8	438	—	—	286	3.59	0.387	73.4 ± 0.7
FP5S10	3.540	—	—	—	—	—		425	558	584	398	1.19	0.386	—
FP0S15	3.544	—	—	—	—	—		387	465	468	—	—	0.383	—

All glasses exhibit comparably low refractive indices, in the range of 1.46–1.49, with Abbe's numbers within 69–89, that is, in the region between phosphate and fluoride-crown. Shifting from FP to FPS results in a slightly decreasing refractive index and decreasing Abbe's number.

For material processing and, for example, drawing of optical fibers, the thermal properties of the melt are of fundamental importance. The glass thermal stability is typically estimated from the characteristic temperatures, *i.e.*, the glass transition temperature T_g, the onset-temperature of crystallization T_x, and the temperature of the crystallization peak as found in a DTA scan, T_p (often associated with the maximum crystallization rate). The parameter of $\Delta T = T_x - T_g$ is then taken as the most accessible measure of glass stability, describing the temperature interval within which the super-cooled glass melt can be processed without the risk of immediate crystallization. A value of ΔT above 100 K is typically taken as an indicator of relative thermal stability such as required, *e.g.*, in a fiber drawing process. Fig. 3 displays the DTA curves of the present glasses from which the values of T_g, T_x and T_p were extracted (Table 1). For FP0, FP2, and FP0S15, ΔT is notably below 100 K, reflecting their previously observed tendency to crystallize (Experimental section). Similarly, also FP4 only narrowly reaches a ΔT of around 100 K. When sulfate is added to this composition such as in FP5S10, the glass stability is significantly enhanced. Beyond that, very high stability was found for melts with phosphate above 10 mol% and/or sulfate at or below 7.5 mol%, in which the crystallization peak could not be observed anymore in the employed experimental setting. T_g of the glasses increases significantly from 403 °C to 467 °C with increasing phosphate content, but decreases to 387 °C with the addition of sulfate. This reflects the more covalent character of bonding among the phosphate groups relative to the ionic sulfate units, which are only weakly crosslinked by the cations. In particular, this shows a significant reduction of the melting temperature while maintaining the stability of the sulfate-free glasses.

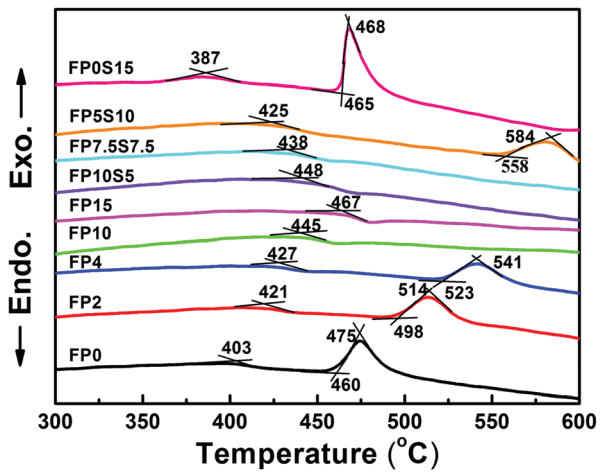

Fig. 3 Differential thermal analyses across the T_g region of FP and FPS glasses and melts.

All physical properties considered here, including glass density, refractive index, transition temperature, crystallization onset temperature, and elastic constants, are directly related to the substitution ratio between phosphate and sulfate.

For doping with transition metal elements, the local chemical properties of the matrix and, in particular, the anionic environment of the dopant are determining factors. The ability of cations to donate an electron is often approximated through mean-field approaches such as the concept of optical basicity Λ_{th}. The value of Λ_{th} is approximated from the weighted sum of the molar contributions of each component,[40]

$$\Lambda_{th} = X(MgF_2)\Lambda(MgF_2) + X(CaF_2)\Lambda(CaF_2) + X(SrF_2)\Lambda(SrF_2) + X(AlF_3)\Lambda(AlF_3) + X(Sr(PO_3)_2)\Lambda(Sr(PO_3)_2) + X(SrSO_4)\Lambda(SrSO_4) \quad (1)$$

where X(i) is the molar fraction of component "i" and Λ(i) is its partial molar optical basicity. In FP glass, with an increase of phosphate content, the optical basicity of the glass increases gradually. Forming FPS by adding sulfate leads to a subsequent decrease in Λ_{th}. Data are summarized in Table 1.

3.2. Structural consideration

A structural model of FP glasses has been formulated on the basis of the ionic fluoride network into which orthophosphate (Q^0) and pyrophosphate (Q^1) groups are incorporated.[41] It has been deducted that preferential over the formation of P–F bonds, the fluorine anion associates with the Al^{3+} cation to form Al–F bonds. This leads to the formation of mixed chains of $Al(O,F)_6$ and PO_4 tetrahedra. FP glasses thus present a transition from an ionic fluoride ensemble to the polymer-like phosphate

 This journal is © The Royal Society of Chemistry 2017

Open Access Article. Published on 27 June 2017. Downloaded on 8/31/2025 5:52:32 AM.
This article is licensed under a Creative Commons Attribution-NonCommercial 3.0 Unported Licence.

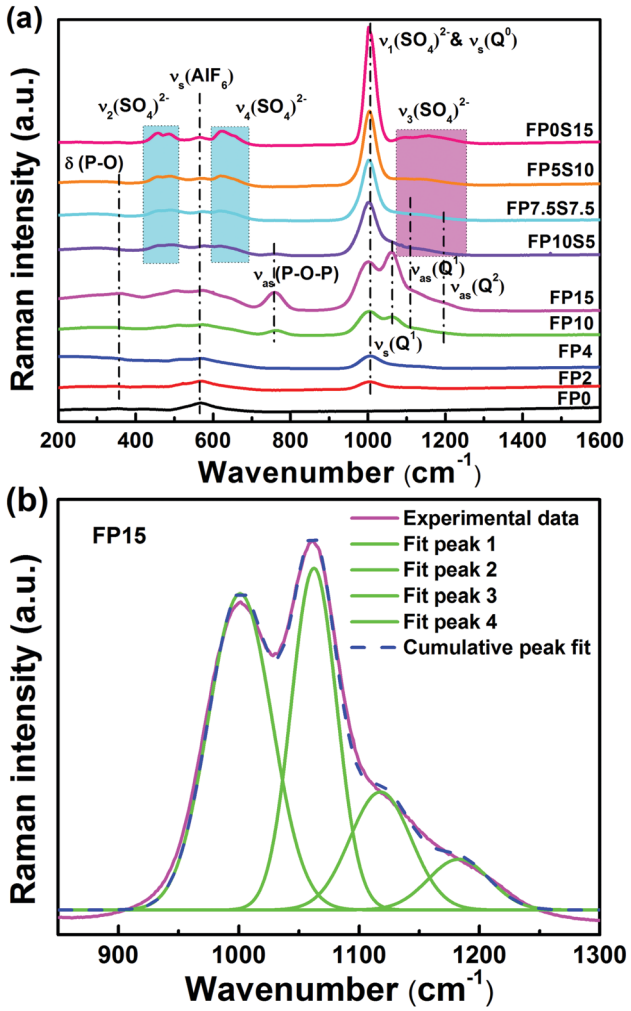

Fig. 4 (a) Raman spectra of the FP and FPS glasses and (b) example of Gaussian deconvolution on FP15 (see the text for assignment details).

network. When additional sulfate groups are introduced, the glass structure becomes more complex. In Fig. 4, Raman spectra of some FP and FPS glasses are shown to illustrate this argument. Bands were assigned on the basis of ref. 42. In addition, the broad signal at 568 cm^{-1} (in FP0) is attributed to the symmetric stretching vibration of the AlF_6 octahedron.[40] With an increase of phosphate content and a decrease of aluminum fluoride content, this peak becomes weaker and broadens due to the formation of $Al(F,O)_6$ octahedra, thereby increasing the overlap with the bending vibrations of phosphate groups in the low frequency range. In brief, on the FP series, the expected gradual increase in network polymerization is clearly seen with the increase of Q^1 and Q^2 – related contributions to the vibrational spectrum (*i.e.*, increasing fraction of bridging oxygen species). Exemplary deconvolutions of the spectral region of 850–1300 cm^{-1} are shown for FP15 in Fig. 4(b). That is, this broad Raman band is best fitted by four Gaussian functions with peaks at 1001 cm^{-1}, 1062 cm^{-1}, 1109 cm^{-1}, and 1194 cm^{-1}. These correspond to the symmetric and asymmetric stretching modes $\nu_s(Q^0)$, $\nu_{s/as}(Q^1)$ and $\nu_{as}(Q^2)$, respectively. Sulfate for phosphate substitution leads to bands evolving around 470 cm^{-1}, 624 cm^{-1}, 1000 cm^{-1} and 1157 cm^{-1}, assigned to $\nu_2(SO_4)^{2-}$, $\nu_4(SO_4)^{2-}$, $\nu_1(SO_4)^{2-}$ and $\nu_3(SO_4)^{2-}$.[22,25] Noteworthily, no Raman signal could be detected in the spectral region around 840–850 cm^{-1}, which would indicate the presence of P–F bonding.[40] In addition, it can be seen that the maximum phonon energy of the present glass increases from 1001 cm^{-1} to 1157 cm^{-1}. A lower phonon energy can increase the radiative transition probability of ions.

3.3. Luminescence properties and crystal field parameters

Photoluminescence (PL) spectra of Cr-doped FP and FPS glasses are shown in Fig. 5. A broad emission band centered at 734 nm is observed in cast glasses, resulting from the spin-allowed $^4T_2 \rightarrow {}^4A_2$ transition in Cr^{3+}.[12,13,15] Differing from this, a very intense emission band is detected in the quenched samples of FP0 and FP0S15 at ~694 nm (corresponding to the *R*-line). This band originates from the spin-forbidden transition of Cr^{3+}: $^2E \rightarrow {}^4A_2$. The accompanying broader background emission (700–900 nm) is attributed to the phonon sidebands of the $^4T_2 \rightarrow {}^4A_2$ transition. There is a positive correlation between the emission intensity and optical basicity. As the glass optical basicity increases with increasing phosphate content, also the emission intensity gradually increases. Similar behaviour was found in chromium-doped silicate glasses.[43] Noteworthily, potential interference through the effect of "photon trapping" on luminescence spectra and decay times is negligible because the samples used for spectroscopic tests are very thin. This is further confirmed by comparing the spectroscopic characteristics for different sample sizes (see Fig. S2 in the ESI†). Noteworthily, the full width at half maximum (FWHM) of the sharp peak at 694 nm is about 83 nm, which is much broader than what is typically observed in Cr^{3+}-doped crystals or glass ceramics.[44] The inhomogeneous broadening of the *R* line reflects the higher versatility of states which is available for Cr^{3+} precipitation, where each individual state provides slight differences in crystal-field splitting.[45,46] Besides the Cr^{3+} ion, also other chromium species exhibit red photoemission in some glasses. For example, Herren *et al.* observed a red emission at ~671 nm (14 900 cm^{-1}) in Cr-doped silica glass

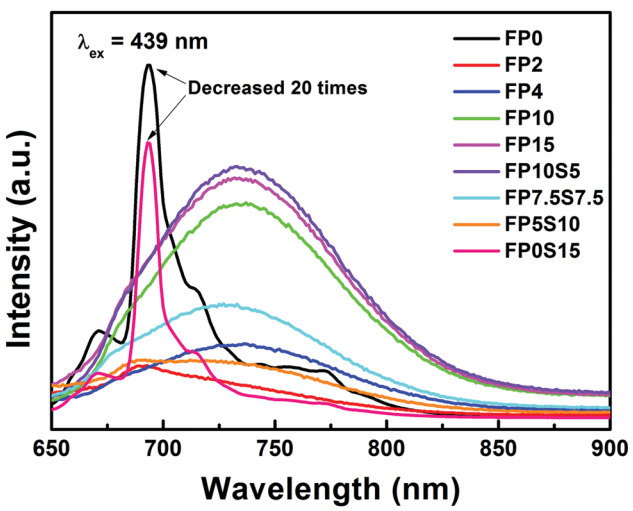

Fig. 5 PL spectra of FP and FPS glasses doped with 0.05 mol% Cr_2O_3.

Open Access Article. Published on 27 June 2017. Downloaded on 8/31/2025 5:52:32 AM.
This article is licensed under a Creative Commons Attribution-NonCommercial 3.0 Unported Licence.

which was prepared through a sol–gel method. They ascribed their observation to the presence of Cr^{5+} ions.[47] Later, the same authors specified this interpretation with a new assignment, *i.e.*, to the ligand-metal charge transfer (LMCT) transitions of Cr^{6+} ions.[48,49] They also ascribed the red band of chromium-doped sol–gel silica glass to Cr^{6+} ions being associated with Cr^{3+}, Cr^{4+} and Cr^{5+} centers.[50] Strk *et al.* obtained a red emission at 655 nm in Cr-doped silica sol–gel glasses (with excitation bands at 280 nm, 400 nm, and 500 nm).[51] Assisted through electron paramagnetic resonance spectroscopy, they proposed a charge-compensation mechanism and attributed the emission band to pairs of Cr^{6+} and Cr^{5+} ions. Clearly, both observations indicate the complexity in assigning the red emission band to either Cr^{3+} or Cr^{6+}, without a final resolution at this point.

Photoluminescence excitation (PLE) spectra of the representative FP10S5 and FP0 glasses are provided in Fig. 6. Monitoring the emission at 734 nm in FP10S5, a continuous envelope with individual bands centered at 287 nm, 425 nm, and 600 nm is observed, originating from the $^4A_2 \rightarrow {}^4T_1(^4P)$, $^4A_2 \rightarrow {}^4T_1(^4F)$, and $^4A_2 \rightarrow {}^4T_2(^4F)$ transitions of Cr^{3+}, respectively.[44] The PLE spectra of the other cast samples are similar to this. Noteworthily, the excitation peaks occur at somewhat shorter wavelengths as compared with the absorption spectra. This signifies that the low-field Cr^{3+} ions have lower luminescence efficiency.[52] Another important point is that the emission position and intensity show high correlations with the excitation wavelength, which moves to a higher wavelength (*e.g.*, from 648 nm to 734 nm) upon increasing the excitation wavelength (from 287 nm to 600 nm). Also for FP0, the PLE spectrum (monitored at 694 nm emission) consists of three broad excitation bands, here at 260 nm, 404 nm, and 540 nm, corresponding to the same transitions as above. The blue-shift relative to FPS is due to a stronger crystal field surrounding the chromium ions. Upon excitation at either of the three peak wavelengths, the position of the emission spectra remains unchanged except for the difference in intensity. An interesting point is that the emission spectra now narrow-down to a sharp line at 694 nm with a FWHM of only 4 nm, largely because of the inhomogeneous distribution of microcrystals in the quenched samples of FP0 and FP0S15.

Fig. 7 depicts the luminescence decay curves of the cast and quenched samples. The observed emission dynamics clearly deviate from a double-exponential decay function, which is taken as a result of multi-site distribution or interaction among Cr^{3+} species in the glass.[45] The average lifetime of the 734 nm emission in cast samples lies within 39.7 μs to 34.5 μs. This is much higher than what has previously been observed on Cr^{3+}-doped phosphate glass (15 μs).[12] For the quenched samples of FP2 and FP5S10, the lifetimes of the sharp emission band at 694 nm reach about 311 μs and 74.5 μs, respectively. In FP0 and FP0S15, they increase further to ~1.06 ms and 1.07 ms, respectively, but are still somewhat lower than in Cr^{3+}-doped silicate glass ceramics (2.45 ms).[44] The latter observation clearly confirms that in the quenched samples, Cr^{3+} precipitates in a crystalline environment.

The Tanabe–Sugano diagram is frequently used to analyze the energy level scheme of Cr^{3+} ($[Ar]3d^3$). For this, crystal field parameter D_q and Racah parameter B can be estimated according to[53]

$$D_q = \frac{E(^4A_2 \rightarrow {}^4T_2)}{10} \quad (2)$$

$$\frac{D_q}{B} = \frac{15(m-8)}{(m^2-10m)} \quad (3)$$

$$m = \frac{E(^4A_2 \rightarrow {}^4T_1) - E(^4A_2 \rightarrow {}^4T_2)}{D_q} \quad (4)$$

where m is determined from the resonance energy of the $^4A_2 \rightarrow {}^4T_1$ and $^4A_2 \rightarrow {}^4T_2$ transitions. Generally, the region of intermediate octahedral fields, $2.1 < D_q/B < 2.3$, was defined to separate the low-field and high-field regions.[54] In the cast glasses, the D_q, B, and D_q/B values are around 1560 cm^{-1}, 760 cm^{-1} and 2.1, respectively, whereas in the quenched samples,

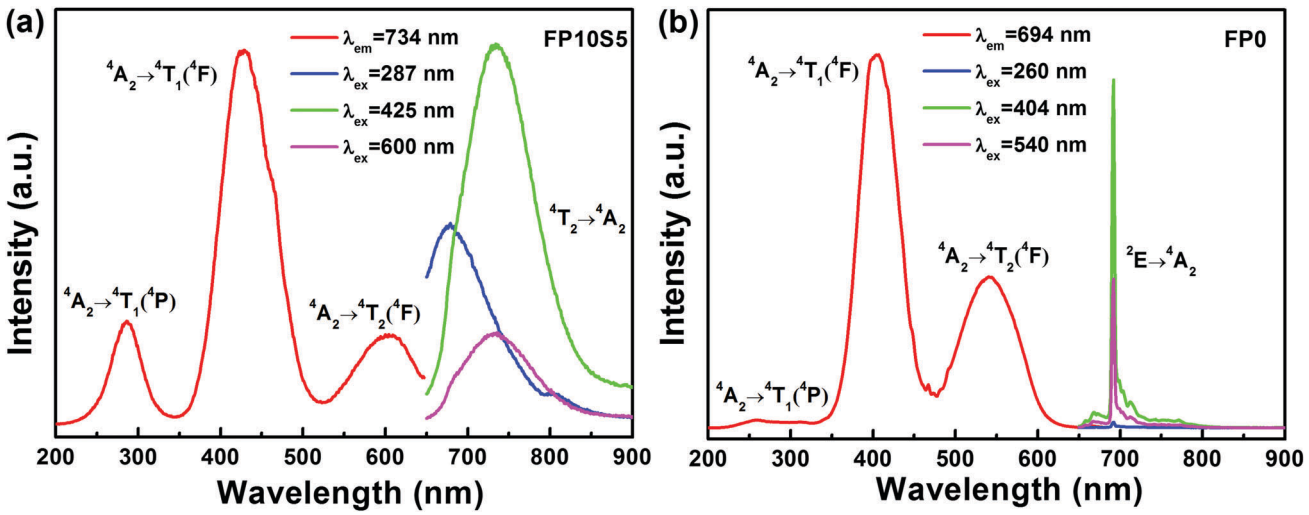

Fig. 6 PLE and PL spectra of selected (a) FP10S5 and (b) FP0 glasses doped with 0.05 mol% Cr_2O_3.

 This journal is © The Royal Society of Chemistry 2017

Open Access Article. Published on 27 June 2017. Downloaded on 8/31/2025 5:52:32 AM.
This article is licensed under a Creative Commons Attribution-NonCommercial 3.0 Unported Licence.

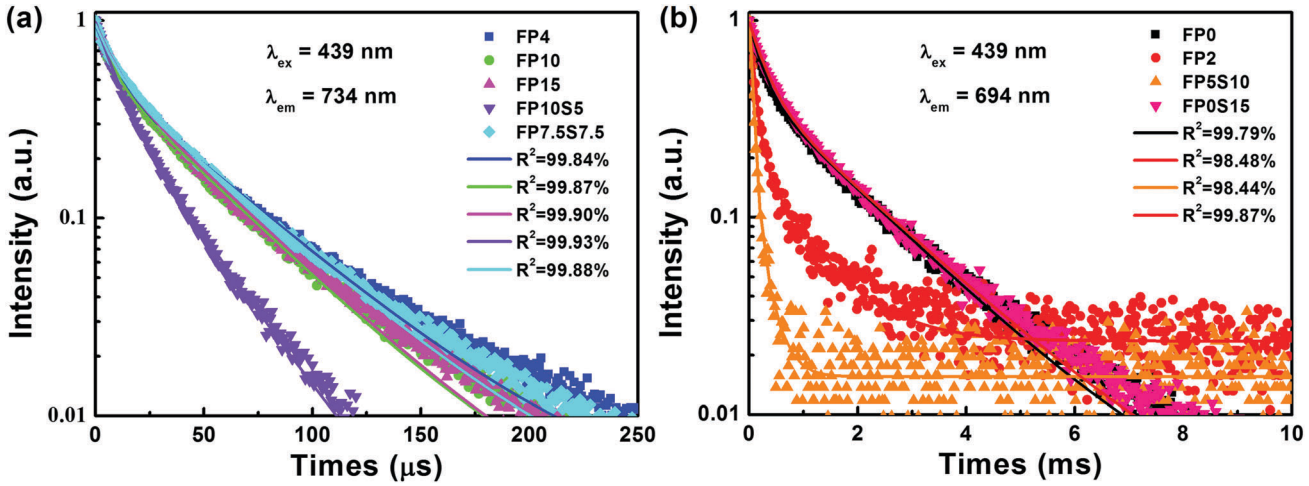

Fig. 7 Luminescence decay curves of Cr^{3+}-doped (a) casting samples and (b) quenching samples.

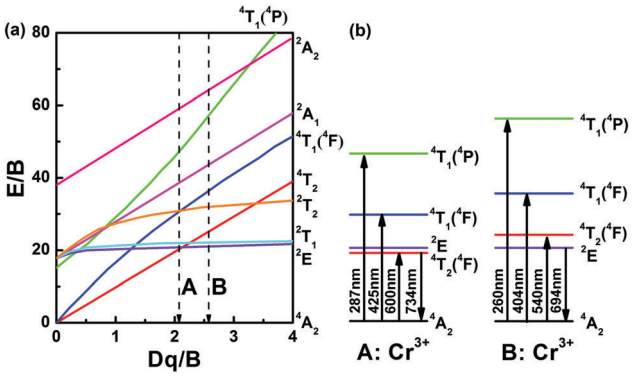

Fig. 8 (a) Tanabe–Sugano diagram and (b) energy level diagram of Cr^{3+}-doped FP and FPS glasses. Labels A and B represent the position of calculated D_q/B in FP10S5 and FP0 samples, respectively.

the values were found to be 1640 cm^{-1}, 630 cm^{-1} and 2.6. This means that the crystal field changes from a low-field to a high-field configuration as a result of varying glass compositions and quenching. We denote the two different situations as (A) and (B), as shown in Fig. 8. As can be readily seen, the $^4T_2$ state is very sensitive to D_q/B while the ^2E state is just the opposite. In situation (A), the Cr^{3+} ion locates in a lower ligand field environment, so the $^4T_2$ level is lower than the ^2E level, which results in broadband emission arising from the spin-allowed $^4T_2 \rightarrow {}^4A_2$ transition. In contrast, when the Cr^{3+} ions locate in the high crystal field (situation (B)), the ^2E level falls below the $^4T_2$ level and, thus, the spectra exhibit a sharp *R*-line originating from the spin-forbidden $^2E \rightarrow {}^4A_2$ transition.

4. Conclusions

In summary, we reported on unusually stable multi-anion glasses of the fluoride-sulfophosphate type (FPS) as a new host material for optically active cation species. Despite a notoriously low polymerization grade, anion mixing in this glass system enables the facile manufacture of bulk or fiber devices which combine several advantages of fluoride and phosphate glasses while using the stabilizing effect of sulfate added. Using the example of chromium doping, we demonstrate a broad red photoluminescence at 734 nm and an inhomogeneous broadening of the *R*-line at 694 nm, originating from the $^4T_2 \rightarrow {}^4A_2$ and $^2E \rightarrow {}^4A_2$ transitions of Cr^{3+}, respectively. The luminescence mechanism was further analyzed on the basis of the corresponding Tanabe–Sugano diagram. Tailored through chemical composition, internally nucleated precipitation of a nanocrystalline fluoride phase enables switching between high-field and low-field configurations of the Cr^{3+} ion, resulting in the specific emission properties and setting the path towards FPS-based optical devices, in particular, broadband tunable fiber amplifiers and lasers.

Acknowledgements

This project has received funding from the European Research Council (ERC) under the European Union's Horizon 2020 research and innovation programme (ERC grant UTOPES, grant agreement no. 681652). W. C. Wang gratefully acknowledges the Chinese Scholarship Council for personal support. We thank our colleagues C. Zeidler, N. Buchert, S. Fuhrmann, C. Siedler and Y. Ding for help with sample preparation and data acquisition.

References

1 G. Boulon, *Opt. Mater.*, 2012, **34**, 499.
2 M. Yasin, S. W. Harun and H. Arof, *Selected Topics on Optical Fiber Technology*, InTech, 2012.
3 T. H. Maiman, *Nature*, 1960, **187**, 493.
4 C. R. Pollock, D. B. Barber, J. L. Mass and S. Markgraf, *IEEE J. Sel. Top. Quantum Electron.*, 1995, **1**, 62.
5 S. B. Mirov, V. V. Fedorov, I. S. Moskalev and D. V. Martyshkin, *IEEE J. Sel. Top. Quantum Electron.*, 2007, **13**, 810.

Open Access Article. Published on 27 June 2017. Downloaded on 8/31/2025 5:52:32 AM.
This article is licensed under a Creative Commons Attribution-NonCommercial 3.0 Unported Licence.

6 M. Mond, D. Albrecht, E. Heumann, G. Heumann, G. Huber and S. Kück, *Opt. Lett.*, 2002, **27**, 1034.
7 J. C. Chen, Y. S. Lin, C. N. Tsai, K. Y. Huang, C. C. Lai, W. Z. Su, R. C. Shr, F. J. Kao and T. Y. Chang, *IEEE Photonics Technol. Lett.*, 2007, **19**, 595.
8 D. G. Deng, H. P. Ma, S. Q. Xu, Q. Wang, L. H. Huang, S. L. Zhao, H. P. Wang and C. X. Li, *J. Opt. Soc. Am. B*, 2010, **27**, 1659.
9 U. R. Rodríguez-Mendoza, V. Lavín, I. R. Martín and V. D. Rodríguez, *J. Lumin.*, 2004, **106**, 77.
10 H. R. Verdun, L. M. Thomas, D. M. Andrauskas, T. McCollum and A. Pinto, *Appl. Phys. Lett.*, 1988, **53**, 2593.
11 C. Deka, M. Bass, B. H. T. Chai and Y. Shimony, *J. Opt. Soc. Am. B*, 1993, **10**, 1499.
12 E. J. Sharp, J. E. Miller and M. J. Weber, *Phys. Lett. A*, 1969, **30**, 142.
13 T. Murata, M. Torisaka, H. Takebe and K. Morinaga, *J. Non-Cryst. Solids*, 1997, **220**, 139.
14 S. M. Yeh, S. L. Huang, Y. J. Chiu, H. Taga, P. L. Huang, Y. C. Huang, Y. K. Lu, J. P. Wu, W. L. Wang, D. M. Kong, K. Y. Huang, J. S. Wang, P. Yeh and W. H. Cheng, *J. Lightwave Technol.*, 2012, **30**, 921.
15 Z. J. Fang, S. P. Zheng, W. C. Peng, H. Zhang, Z. J. Ma, S. F. Zhou, D. P. Chen and J. R. Qiu, *J. Am. Ceram. Soc.*, 2015, **98**, 2772.
16 M. J. Weber, *J. Non-Cryst. Solids*, 1990, **123**, 208.
17 J. H. Campbell and T. I. Suratwala, *J. Non-Cryst. Solids*, 2000, **263**, 318.
18 S. Tanabe, *C. R. Chim.*, 2002, **5**, 815.
19 K. Griebenow, U. Hoppe, D. Möncke, E. I. Kamitsosc and L. Wondraczek, *J. Non-Cryst. Solids*, 2017, **460**, 136.
20 B. P. Rodrigues, J. Deubener and L. Wondraczek, *Front. Mater.*, 2016, **3**, 25.
21 K. Griebenow, E. I. Kamitsos and L. Wondraczek, *J. Non-Cryst. Solids*, 2017, **468**, 74.
22 N. Da, O. Grassmé, K. H. Nielsen, G. Peters and L. Wondraczek, *J. Non-Cryst. Solids*, 2011, **357**, 2202.
23 N. Da, S. Krolikowski, K. H. Nielsen, J. Kaschta and L. Wondraczek, *J. Am. Ceram. Soc.*, 2010, **93**, 2171.
24 S. Sirotkin, R. Meszaros and L. Wondraczek, *Int. J. Appl. Glass Sci.*, 2012, **3**, 44.
25 D. Möncke, S. Sirotkin, E. Stavrou, E. I. Kamitsos and L. Wondraczek, *J. Chem. Phys.*, 2014, **141**, 224509.
26 S. Reibstein, N. Da, J. P. Simon, E. Spiecker and L. Wondraczek, *Phys. Chem. Glasses*, 2012, **53**, 61.
27 D. Ehrt and T. Töpfer, *Proc. SPIE*, 2000, **4102**, 95.
28 J. F. Philipps, T. Töpfer, H. Ebendorff-Heidepriem, D. Ehrt and R. Sauerbrey, *Appl. Phys. B: Lasers Opt.*, 2001, **72**, 399.
29 H. Ebendorff-Heidepriem, D. Ehrt, M. Bettinelli and A. Speghini, *J. Non-Cryst. Solids*, 1998, **240**, 66.
30 S. Tanabe, S. Yoshii, K. Hirao and N. Soga, *Phys. Rev. B*, 1992, **45**, 4620.
31 J. J. Zhang, D. B. He, Z. C. Duan, L. Y. Zhang, S. X. Dai and L. L. Hu, *Laser & Optronics Prog.*, 2005, **42**, 12.
32 L. Y. Zhang, L. Wen, H. T. Sun, J. J. Zhang and L. L. Hu, *J. Alloys Compd.*, 2005, **391**, 156.
33 P. Ebeling, D. Ehrt and M. Friedrich, *Phosphorus Res. Bull.*, 1999, **10**, 484.
34 G. A. Kumar, A. Martinez and E. De la Rosa, *J. Lumin.*, 2002, **99**, 141.
35 G. A. Kumar, E. De la Rosa, A. Martinez, N. V. Unnikrishnan and K. Ueda, *J. Phys. Chem. Solids*, 2003, **64**, 69.
36 Q. H. Le, D. Möncke, E. I. Kamitsos and L. Wondraczek, *Society of Glass Technology (SGT) Centenary Conference*, 2016.
37 S. Emura, H. Maeda, Y. Kuroda and T. Murata, *Jpn. J. Appl. Phys.*, 1993, **32**, 734.
38 J. Ueda and S. Tanabe, *J. Am. Ceram. Soc.*, 2010, **93**, 3084.
39 W. A. Weyl, *Coloured Glasses*, Society of Glass Technology, 2016.
40 L. L. Velli, C. P. E. Varsamis and E. I. Kamitsos, *Phys. Chem. Glasses*, 2008, **49**, 182.
41 D. Möncke, D. Ehrt, L. Velli, C. P. E. Varsamis and E. I. Kamitsos, *Int. Congr. Glass, Proc., 20th*, 2004.
42 A. Thieme, D. Möncke, R. Limbach, S. Fuhrmann, E. I. Kamitsos and L. Wondraczek, *J. Non-Cryst. Solids*, 2015, **410**, 142.
43 H. Yamazaki and S. Tanabe, *Jpn. J. Appl. Phys.*, 2005, **44**, 5011.
44 D. Q. Chen, Z. Y. Wan and Y. Zhou, *Opt. Lett.*, 2015, **40**, 3607.
45 F. Rasheed, K. P. D'onnell, B. Henderson and D. B. Hollis, *J. Phys.: Condens. Matter*, 1991, **3**, 1915.
46 S. V. Bulyarskii, A. E. Kozhevin, S. N. Mikov and V. V. Prikhodko, *Phys. Status Solidi A*, 2000, **180**, 555.
47 M. Herren, H. Nishiuchi and M. Morita, *J. Chem. Phys.*, 1994, **101**, 4461.
48 M. Moirta, N. Miyazaki, S. Murakami, M. Herren and D. Rau, *J. Lumin.*, 1998, **76&77**, 238.
49 M. Herren, K. Yamanaka and M. Morita, *Tech. Rep. Seikei Univ.*, 1995, **32**, 61.
50 M. Morita, D. Rau, S. Kajiyama, T. Sakurai, M. Baba and M. Iwamura, *Mater. Sci.-Pol.*, 2004, **22**, 5.
51 W. Stręk, P. J. Dereń, E. Łukowiak, J. Hanuza, H. Drulis, A. Bednarkiewicz and V. Gaishun, *J. Non-Cryst. Solids*, 2001, **288**, 56.
52 A. van Die, G. Blasse and W. F. van der Weg, *J. Phys. C: Solid State Phys.*, 1985, **18**, 3379.
53 C. R. Kesavulu, R. P. S. Chakradhar, R. S. Muralidhara, J. L. Rao and R. V. Anavekar, *J. Alloys Compd.*, 2010, **496**, 75.
54 F. Rasheed, K. P. O'Donnell, B. Henderson and D. B. Hollis, *J. Phys.: Condens. Matter*, 1991, **3**, 3825.

 This journal is © The Royal Society of Chemistry 2017